Pd nanocluster-decorated CoFe composite supported on nitrogen carbon nanotubes as a high-performance trifunctional electrocatalyst

Manjunatha Reddy, Li Dong, Zibo Zhai, Jianyi Wang, Qianru Fu, Wei Yan, Jiujun Zhang

KeAi
CHINESE ROOTS
GLOBAL IMPACT

Available online at www.sciencedirect.com

ScienceDirect

Green Energy & Environment 7 (2022) 933–947

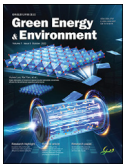

www.keaipublishing.com/gee

Research paper

Pd nanocluster-decorated CoFe composite supported on nitrogen carbon nanotubes as a high-performance trifunctional electrocatalyst

Revanasiddappa Manjunatha [a,b], Li Dong [a,b], Zibo Zhai [a], Jianyi Wang [a], Qianru Fu [a], Wei Yan [a,*], Jiujun Zhang [a,*]

[a] *Institute for Sustainable Energy/College of Sciences, Shanghai University, Shanghai, 200444, China*
[b] *Zhaoqing Leoch Battery Technology Co. Ltd., Zhaoqing, 518000, China*

Received 14 August 2020; revised 30 November 2020; accepted 8 December 2020
Available online 11 December 2020

Abstract

Rational design and synthesis of low-cost trifunctional electrocatalysts with improved stability and superior electrocatalytic activity for oxygen reduction reaction (ORR), oxygen evolution reaction (OER), and hydrogen evolution reaction (HER) are highly desirable but remain as the bottlenecks at the current state of technology. In this paper, the cobalt-iron (Co–Fe) composite supported on nitrogen-doped carbon nanotubes (CoFe composite/NCNTs) is synthesized. The intrinsic OER and HER catalytic activities of this CoFe composite/NCNTs composite are significantly improved with palladium (Pd) nanocluster decoration [Pd-coated (CoFe composite/NCNTs)]. The as-prepared Pd-coated (CoFe composite/NCNTs) catalyst exhibits excellent trifunctional electrocatalytic activity and stability due to the interfacial coupling between Pd and (CoFe composite/NCNTs). This catalyst is successfully employed in the water electrolysis cell as both OER and HER electrode catalysts, flexible rechargeable Zn-air battery as the bifunctional ORR and OER electrode catalyst. The cell voltage of this catalyst-coated electrodes requires only 1.60 V to achieve 10 mA cm^{-2} current density for water electrolysis cell, which is comparable to and even better than that of Pt/C and Ir/C based cell. The primary Zn-air battery using this catalyst shows a constant high open-circuit voltage (OCV) of 1.47 V and a maximum power density of 261 mW cm^{-2} in the flooded mode configuration. Most importantly, a flexible Zn-air battery with this catalyst runs very smoothly without a change in voltage gap during flat, bending, and twisting positions.

Keywords: Zinc-air battery; Water electrolysis; Palladium; Composite; Trifunctional catalyst

1. Introduction

The development of multifunctional electrocatalysts that can catalyze all three important electrochemical reactions, namely, oxygen reduction reaction (ORR), oxygen evolution reaction (OER), and hydrogen evolution reaction (HER) are indeed important and gaining a great deal of research interests. Multifunctionality of the catalyst is one of the simple ways to reduce the overall cost of catalysts required for clean and sustainable energy storage and conversion devices such as metal-air batteries, fuel cells and water electrolysis [1–4]. Currently, noble metals-based materials such as platinum-iridium- and ruthenium-based catalysts have been using as a state-of-the-art catalyst for ORR/HER and OER, respectively [5,6]. However, due to high cost and low abundance, these precious metals are non-conducive to large-scale practical applications [5,6]. Therefore, developing alternative multifunctional electrocatalysts with low-cost, high activity, and long-term stability is necessary.

Among different types of non-precious metal catalysts, the layered double hydroxides (LDHs) as a kind of two-dimensional inorganic layered materials consisting of positively

* Corresponding authors.
E-mail addresses: yveayan@shu.edu.cn (W. Yan), jiujun.zhang@i.shu.edu.cn (J. Zhang).

https://doi.org/10.1016/j.gee.2020.12.005

charged brucite-type host layers and exchangeable charge-balancing interlayer anions have been explored recently [7]. Through incorporating various metal ions without changing the structure as well as anion exchange properties, LDHs with special features can be prepared, which opens up their applications in different fields [8].

As per the water electrolysis is concerned, LDHs are known for their better electrocatalytic activity, and in some cases, they could outperform the state-of-the-art catalysts in alkaline media. For instance, Bhowmik et al. [9] reported that a CoFe LDH supported on graphitic carbon nitride to form a composite electrocatalyst, which exhibited a superior OER activity than the commercial IrO_2 catalyst. This composite catalyst showed a high electrochemical surface area, easily available abundant active sites, and ease of mass transport owing to its two-dimensional sheet morphology accounted for the enhanced activity. Similarly, NiFe LDH also showed excellent water oxidation ability in alkaline conditions [10–12]. Liu et al. [13] illustrated that the delamination and exfoliation of CoFe LDH could improve intrinsic electrical conductivity as well as the formation of more coordinative unsaturated metal sites for enhancing the catalytic performance of overall water splitting. Amorphization [14], variation of metal ions Co/Fe ratios [15], and small changing Pd loading content [16] of CoFe LDH could significantly boost its water oxidation performance. In addition, Song et al. [17] prepared highly active, stable, and ultrathin CoMn LDH nanoplates for water oxidation.

Regarding metal-air batteries, zinc (Zn)-air batteries, as well as all-solid-state flexible Zn-air counterparts [19], have been gaining popularity due to their low-cost, high theoretical specific energy density (1084 Wh kg^{-1}), the abundance of Zn, and their intrinsic safety [18,19]. Despite these several advantages, the rechargeable Zn-air batteries have not been commercialized yet till today, and a considerable amount of research effort is still needed to realize their practical applications. Recently, various types of bifunctional catalysts were employed to improve the rechargeability of Zn-air batteries, such as heteroatom doped carbon [20–25], metal oxides [18,19,26–32], alloys [33–35], metal nitride [36], and LDH [37]. Besides, some strategies were employed to avoid corrosion of Zn during the charge–discharge process and to increase battery life. For example, Schmid et al. [38] reported that the incorporation of bismuth oxide with Zn powder could significantly improve rechargeability due to an increase in Zn utilization. Similarly, Da et al. [39] showed that the addition of ultrafine bismuth powder to the Zn electrode could not only subdue the self-corrosion rate in alkaline medium but also suppress dendrite growth by improving the uniformity of current density distribution on the electrode surface. Furthermore, some organic compounds are added into the electrolyte to retard the corrosion of anode [40].

In this paper, a facile strategy is employed for the synthesis of CoFe composite supported on nitrogen-doped carbon nanotubes (NCNTs) by a simple hydrothermal method. NCNTs can provide mechanical support to CoFe composite but also being conducive to improve the electrical conductivity, which in turn enhance the electrocatalytic performance. Decoration of Pd nanocluster on such a CoFe composite/NCNTs catalyst further leads to the trifunctional electrocatalytic activities for ORR, OER, and HER. The as-prepared electrocatalyst shows superior ORR ($E_{1/2}$ = 828 mV), OER (η_{j10} = 285 mV), and appreciable HER (η_{j10} = 214 mV) activities in alkaline media. This catalyst is used in water splitting cell, primary and rechargeable Zn-air batteries to realize its practical applications. The primary Zn-air battery delivers a constant high OCV of 1.47 V for up to 12 h and a maximum power density of 261 mW cm^{-2} in the flooded mode configuration. A rechargeable Zn-air battery shows a low voltage gap of 0.69 V at a charge–discharge current density of 10 mA cm^{-2}. Indeed, this catalyst-based all-solid-state flexible Zn-air battery can give a remarkable 250 charge–discharge cycles in an air-breathing mode. Thus, outstanding ORR, OER, and HER activities of such a catalyst are attributed to the increased catalytically active sites in the presence of a trace amount of Pd, strong electric interaction, and the improved charge transfer between Pd nanoclusters and CoFe composite/NCNTs. Although CoFe LDH was used as a precursor to synthesize Co, Fe based bimetallic and oxides for rechargeable Zn-air battery application [41], metal nanocluster decorated CoFe composite is not yet explored as a trifunctional catalyst. To the best of our knowledge, this is the first Pd nanocluster anchored CoFe composite/NCNTs electrocatalyst as a trifunctional electrocatalyst and its applications in both water electrolysis cell and flexible reachable Zn-air battery.

2. Experimental section

2.1. Reagents

$Co(NO_3)_2{\cdot}6H_2O$, $Fe(NO_3)_3{\cdot}9H_2O$, $Pd(NO_3)_2$, potassium hydroxide, zinc acetate, sodium carbonate, sodium hydroxide, aqueous ammonia (30%), sodium borohydride, and polyvinyl alcohol (PVA) were purchased from Aladdin Chemical Corp. Other chemicals used in the experiments were of analytical grade and used without further purification. All aqueous solutions were prepared in Millipore water (Milli-Q system).

2.2. Synthesis of Pd-coated (CoFe composite/NCNTs)

The Pd-coated (CoFe composite/NCNTs) catalyst was synthesized in three different steps. firstly, the nitrogen-doped carbon nanotubes (NCNTs) were prepared by using the procedure given elsewhere [42]. In brief, the oxidized CNTs (46 mg) were dispersed in 20 mL of Milli-Q water, followed by the addition of 0.5 mL of ammonia solution. Subsequently, this reaction mixture was transferred into the hydrothermal bomb and heated at 180 °C for 12 h to obtain NCNTs. However, prior to nitrogen doping, the oxidized CNTs were prepared as per the procedure given by Xiao et al. [43]. In the second step, the CoFe composite was further composited with NCNTs to form a catalyst synthesized by a simple coprecipitation method followed by hydrothermal treatment. In detail, 50 mg of NCNTs dispersed in 20 mL of water by

ultrasonication for 20 min. Then, $Co(NO_3)_2{\cdot}6H_2O$ (40 mmol L^{-1}) and $Fe(NO_3)_3{\cdot}9H_2O$ (20 mmol L^{-1}) salts were dissolved to form a slurry. 20 mL water containing Na_2CO_3 (13 mmol L^{-1}) and NaOH (150 mmol L^{-1}) salts was added dropwise to this resultant slurry under vigorous stirring (900 r min^{-1}). After completing the addition, the reaction was continued for additional 20 min, followed by hydrothermal treatment at 100 °C for 24 h. The resulting product was filtered, washed with water, and dried at 50 °C under vacuum overnight to form CoFe composite/NCNTs sample. The third and final step involved a dispersion of 50 mg CoFe composite/NCNTs sample in 50 mL of water by using ultrasonication for 30 min to form a uniform slurry. Then, 1 mL of $Pd(NO_3)_2$ (3 wt%) was introduced dropwise, followed by 5 mL of $NaBH_4$ (6 mmol L^{-1}) added very slowly for 20 min, and then the reaction was kept for another 1 h. Finally, Pd-coated (CoFe composite/NCNTs) catalyst was filtered and washed with plenty of water and dried at 50 °C under vacuum overnight. Scheme 1 shows above mentioned procedure.

2.3. Material characterization

The powder X-ray diffraction (XRD) measurements were carried out with a Rigaku Dmax-2200 instrument using Cu Kα (λ = 1.54 Å) radiation source. The morphology of the as-synthesized materials was examined using field-emission scanning electron microscopy (FESEM; JEOL, JSM-7500F), transmission electron microscopy (TEM, JEM-200 CX, JEOL), and high-resolution TEM (HRTEM, JEM-2100F JEOL Inc.). Elemental mapping was performed using energy-dispersive X-ray spectroscopy (EDX) equipped with the TEM. The surface chemical bonds and valence states of the as-prepared electrocatalysts were determined using X-ray photoelectron spectroscopy (XPS, Thermo Fisher Scientific K-Alpha spectrometer using Al Kα X-ray radiation). In the present work, the binding energies (BE) were calibrated by setting the measured BE of C 1s to 284.8 eV. The elemental composition of electrocatalysts was determined using an ICP-OES (PerkinElmer 8300) with high-purity argon (99.9999). For sample preparation of ICP-OES studies, 10 mg of sample was accurately weighed and placed into 50 mL Teflon tube. 4 mL of aqua regia (1 mL of HNO_3 and 3 mL of HCl) was added into the tube and allowed sufficient time to dissolve metals from the carbon. The proper filtrations and dilutions were made before ICP- OES experiments.

2.4. Electrochemical measurements

The electrochemical tests were carried out by using a CHI 760E electrochemical workstation (CH Instrument, Shanghai) with a three-electrode system. A conventional three-electrochemical cell was employed to measure the electrocatalyst performance, in which a glassy carbon electrode coated with the as-prepared catalyst as the working electrode, a Pt foil as the counter electrode, and a Hg/HgO (MMO) as the reference electrode, respectively. The catalyst ink was prepared by dispersing 5 mg of the catalyst in 0.5 mL of the isopropanol-water mixture (1:1) along with 20 μL of 5 wt% Nafion®. The slurry was then homogenized by ultrasonication for 30 min 2 μL of the ink was drop-casted onto the glassy carbon electrode of 3 mm diameter to obtain the working electrode with a catalyst loading of 0.27 mg cm^{-2}. All the measured electrode potentials were vs. MMO was converted into the reported electrode potentials vs. the reversible hydrogen electrode (RHE) in this paper. ORR measurements were carried out in N_2- or O_2-saturated 0.1 mol L^{-1} KOH at a scan rate of 10 mV s^{-1}. Whereas, OER and HER measurements were performed in 1.0 mol L^{-1} KOH with the aforementioned conditions. A steady blanket of O_2 was maintained above the KOH electrolyte during the ORR experiments.

The number of electrons transferred per oxygen molecule during ORR was calculated using The Koutecky–Levich (K-L) equation as given below:

$$\frac{1}{j}=\frac{1}{j_L}+\frac{1}{j_K}=\frac{1}{B\omega^{1/2}}+\frac{1}{j_K} \tag{1}$$

$$B=0.62nFC_O D_O^{2/3}\nu^{-1/6} \tag{2}$$

where, ω is the angular velocity, j is the measured current density, j_K and j_L are the kinetic and diffusion-limiting current densities, respectively, n is the number of electrons transferred, F is the Faraday constant (96,485 C mol^{-1}), C_O is the bulk concentration of O_2 (1.2×10^{-6} mol cm^{-3}), D_O is the diffusion coefficient of O_2 (1.9×10^{-5} cm^2 s^{-1}) and υ is the kinematic viscosity of the electrolyte (0.01 cm^2 s^{-1}). B can be obtained from the slope of the K-L equation.

The rotating ring disc electrode (RRDE) experiments were carried out to measure the number of electrons transferred and hydrogen peroxide yield (%H_2O_2) during ORR. The following Eqs. (3) and (4) were used for their calculations.

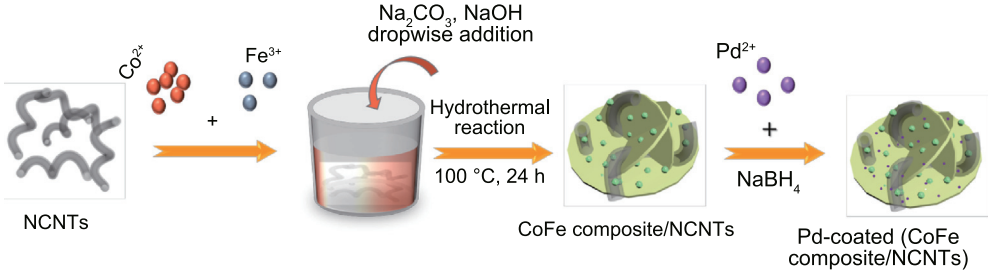

Scheme 1. Synthesis route for the preparation of Pd-coated (CoFe composite/NCNTs).

$$n = \frac{4I_D}{I_D + \left(\frac{I_R}{N}\right)} \quad (3)$$

$$\%H_2O_2 = 200 \times \frac{\frac{I_R}{N}}{I_D + \left(\frac{I_R}{N}\right)} \quad (4)$$

where I_D is the Faradaic current at the disk, I_R is the Faradaic current at the ring, and N is the collection efficiency of the ring (0.37).

2.5. Water splitting tests

The electrocatalyst ink was prepared by dispersing 10 mg of the catalyst in 1 mL of the isopropanol-water mixture (1:1) along with 50 μL of 5 wt% Nafion®. The slurry was ultrasonicated for 30 min to obtain uniform dispersion. The anode and cathode were both carbon papers (1 × 1 cm^2) coated with the catalyst. Catalyst loading of 1 mg cm^{-2} was maintained for both anode and cathode electrodes. Overall water splitting experiment was carried out in a home-made electrochemical cell.

2.6. Fabrication and testing of Zn-air battery

2.6.1. Zn-air battery assembling and testing in the flooded mode configuration

The Zn-air battery was constructed by using the homemade setup, which consists of a Zn foil anode, catalyst loaded carbon paper cathode, and 6.0 mol L^{-1} KOH electrolyte. This two-electrode configuration was used for primary Zn-air battery experiments. Whereas, for a rechargeable battery, a parallel tri-electrode configuration was used with a Zn plate as the electrode located between the two catalyst-coated carbon paper electrodes. For the two carbon paper electrodes, one is located at one side of the Zn plate for the ORR electrode, and the other is located at the other side of the Zn plate as the OER electrode, respectively [44]. In this rechargeable Zn-air battery, an additional 0.2 mol L^{-1} zinc acetate was introduced to the 6.0 mol L^{-1} KOH during charge–discharge studies. The humidified air (5 mL min^{-1}) was continuously fed to the cell during all the experiments.

2.6.2. All-solid-state flexible Zn-air battery assembling and testing in the air-breathing mode

The all-solid-state flexible Zn-air battery was fabricated by sandwiching alkaline gel electrolyte (AGE) between Zn foil anode and catalyst-coated carbon cloth cathode. Carbon cloth served as the catalyst support as well as the current collector. A perforated polyethylene tape was tightly wrapped around the battery to improve its mechanical integrity. To get AGE, 5 g of PVA was dissolved in 50 mL of water. The freshly prepared 3.5 mL of 18.0 mol L^{-1} KOH, 1.5 mL of zinc acetate was added under magnetic stirring. This cocktail was gradually heated to 95 °C and maintained for 45 min. And then, the formed viscous solution was poured on the glass Petridis followed by freezing for 12 h. Finally, the as-prepared AGE was soaked in the KOH and zinc acetate mixture for 12 h before usage.

3. Results and discussion

3.1. Materials characterization and analysis

Fig. 1a shows the powdered X-ray diffraction patterns of CoFe composite/NCNTs (red) and Pd-coated (CoFe composite/NCNTs) (blue) catalysts. The peaks at 2θ values of 11.79°, 23.61°, and 33.23° can be ascribed to the (003), (006) and (009) planes of cobalt-iron layered double hydroxide [15]. Besides, cobalt-iron oxide ($CoFe_2O_4$) peaks at 18.81°, 30.79°, 36.25°, and 44.16° are corresponding to the (111), (220), (311), and (400) lattice planes of cobalt-iron oxide [45]. The peaks corresponding to Pd could not be detected in the final electrocatalyst sample due to its trace amount. The morphology of different CoFe composites was studied by transmission electron microscopy (TEM). Fig. 1b–d are corresponding to the TEM images of CoFe composite, CoFe composite/NCNTs, and Pd-coated (CoFe composite/NCNTs) electrocatalysts, respectively. From TEM images, it is evident that cobalt-iron oxide nanoparticles are distributed across two-dimensional thin CoFe LDH layers forming a unique CoFe composite. The close and subtle inspection of Fig. 1d reveals the formation of small Pd nanoclusters on CoFe composite/NCNTs. The high-resolution TEM images as shown in Fig. 1e and F clearly show the dispersion of small Pd nanoclusters (< 5 nm) on CoFe composite/NCNTs sample. In addition, HRTEM of Fig. 1e illustrates lattice fringes with the lattice distances of 0.29, 0.47, and 0.26 nm, which are corresponding to (220), (111), and (012) planes of cobalt iron oxide and CoFe LDH, respectively.

X-ray photoelectron spectroscopy (XPS) was employed to ascertain chemical oxidation states of the elements present in CoFe composite along with their coupling interactions. XPS survey spectra reveal the presence of Co, Fe, N, O, and C elements in CoFe composite/NCNTs and additional Pd in metal decorated counterpart, as shown in Fig. 2a. Besides, the XPS spectrum was also used to determine the atomic ratio of Co:Fe:Pd:C:N (0.047:0.094:0.023:0.808:0.027) elements present in the catalyst. The high-resolution XPS spectra of Co and Fe are presented in Fig. 2b and c, respectively. From the figures, it is evident that both Co and Fe show doublet ($2p_{1/2}$ and $2p_{3/2}$) due to the spin-orbital coupling [9]. The Co 2p XPS spectra of both samples display the presence of Co^{3+} (ca. 780.5 eV) as well as Co^{2+} (ca. 782.1 eV) species along with their corresponding satellite peaks at ca. 785.9, 803.1 eV and 789.6, 806.8 eV [13]. The oxidation states of Co were measured by integrating the areas of the fitted curves. Interestingly, the relative atomic ratio of Co^{3+}/Co^{2+} on the surface of Pd-coated (CoFe composite/NCNTs) was found to be higher (1.68) than that of CoFe composite/NCNTs counterpart (1.16), suggesting an enhanced oxidation state of Co species after Pd incorporation. Similarly, the Fe 2p XPS spectra of the aforementioned samples show four distinctive peaks at 711.1,

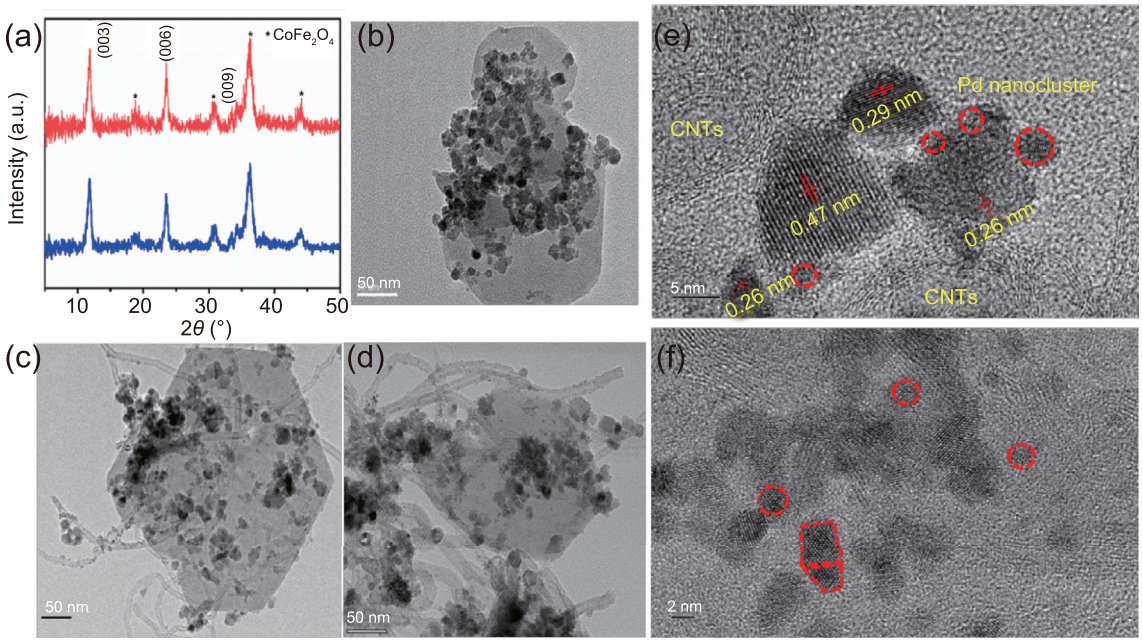

Fig. 1. XRD patterns of CoFe composite/NCNTs and Pd-coated (CoFe composite/NCNTs) (a). TEM images of CoFe composite (b), CoFe composite/NCNTs (c), and Pd-coated (CoFe composite/NCNTs). HRTEM images of Pd-coated (CoFe composite/NCNTs) (e and f).

713.7, 718.2, and 724.5 eV. The peaks at 711.1 and 713.7 eV can be attributed to Fe(III) and Fe(II) ions, respectively, and The peak at 724.5 eV can be attributed to the coexistence of Fe(III) and Fe(II) ions. The common satellite peak for all the aforementioned peaks can be found at 718.2 eV [46]. O 1s XPS spectra were deconvoluted into three peaks, as shown in Fig. 2d. The peaks at ca. 530.1, 531.5, and 533.6 eV can be ascribed to metal–oxygen, hydroxyl-oxygen and carbon-oxygen species, respectively [9]. N 1s and C 1s is XPS spectra were also deconvoluted into three peaks, as shown in Figs. S1A and B, respectively. Peaks at ca. 399.2, 400.5, and 403.9 eV can be designated to pyridinic-N, quaternary-N, and pyridinic-N^{+}-O^{-}, respectively [47]. Whereas, peaks at ca. 284.7, 285.5, and 288.3 eV can be assigned to sp^2 C–C/sp^3 C–C, sp^2 C–N, and sp^3 C–N bonds, respectively [48]. To ascertain the oxidation state of Pd in the Pd-coated (CoFe composite/NCNTs) catalyst, a high-resolution XPS measurement was performed, and the obtained result is shown in Fig. 3a. The $3d_{5/2}$ and $3d_{3/2}$ spectra of Pd can be convoluted and each spectrum consists of two peaks. From the literature, it is a well-known fact that the binding energy values of metallic Pd^0 are 335.2 eV [49,50]. However, the binding energy of Pd present in the catalyst is shifted to 336.0 eV, suggesting that it exists as an oxidized single atom or ultra-small cluster. This result is in good agreement with previous reports [49,50]. Similarly, the typical PdO peak can be found in the range of 336.8 ± 0.2 eV [50]. Thus, the peak at 337.8 eV could not be due to PdO instead it can be attributed to Pd in the surface interaction phase with CoFe composite/NCNTs. Boronin et al. [50] previously explained this kind of interaction in detail. The positional distribution of Pd nanoclusters in Pd-coated (CoFe composite/NCNTs) catalyst is revealed by high-angle annular dark-field scanning TEM (HAADF-STEM) (Fig. 3b and c), energy-dispersive X-ray spectroscopy (EDX) line scanning profile (Fig. 3d), and EDX elemental mapping pattern (Fig. 3e). From these analyses, it is evident that Pd nanoclusters are also formed on the edges of CoFe composite/NCNTs. This result is in good agreement with its HRTEM counterpart (Fig. 1e and f). The atomic compositions of Pd, Co, and Fe present in the Pd-coated (CoFe composite/NCNTs) were also evaluated by ICP-OES measurement. It is found that the catalyst contained 20.1 wt% Co, 9.9 wt% Fe, and 2.8 wt% Pd.

3.2. Electrochemical activity of Pd-coated (CoFe composite/NCNTs) catalyst for ORR, OER and HER

The ORR catalytic activity of NCNTs, CoFe composite/NCNTs, Pd-coated (CoFe composite/NCNTs), and commercial Pt/C (20 wt%) were evaluated by cyclic voltammetry (CV) in O_2-saturated 0.1 mol L^{-1} KOH solution, as shown in Fig. 4a. A well-defined O_2 reduction peak can be observed at an ORR onset potential of 717 mV (vs. RHE) for NCNTs. However, CoFe composite/NCNTs catalyst shows a substantial enhancement in ORR. Precisely, there is a ca. 3-fold increase in reduction current along with 100 mV of decrease in onset potential, illustrating the enhanced ORR activity of CoFe composite/NCNTs than NCNTs. To examine the role of $CoFe_2O_4$ particles in CoFe composite/NCNTs catalyst, $CoFe_2O_4$ particles were synthesized by a hydrothermal method as per the procedure given elsewhere [51] and its structure was confirmed by XRD studies (Fig. S2). The as-prepared $CoFe_2O_4$ particles were physically mixed with NCNTs in a ratio of 2:1 and then its electrocatalytic activity

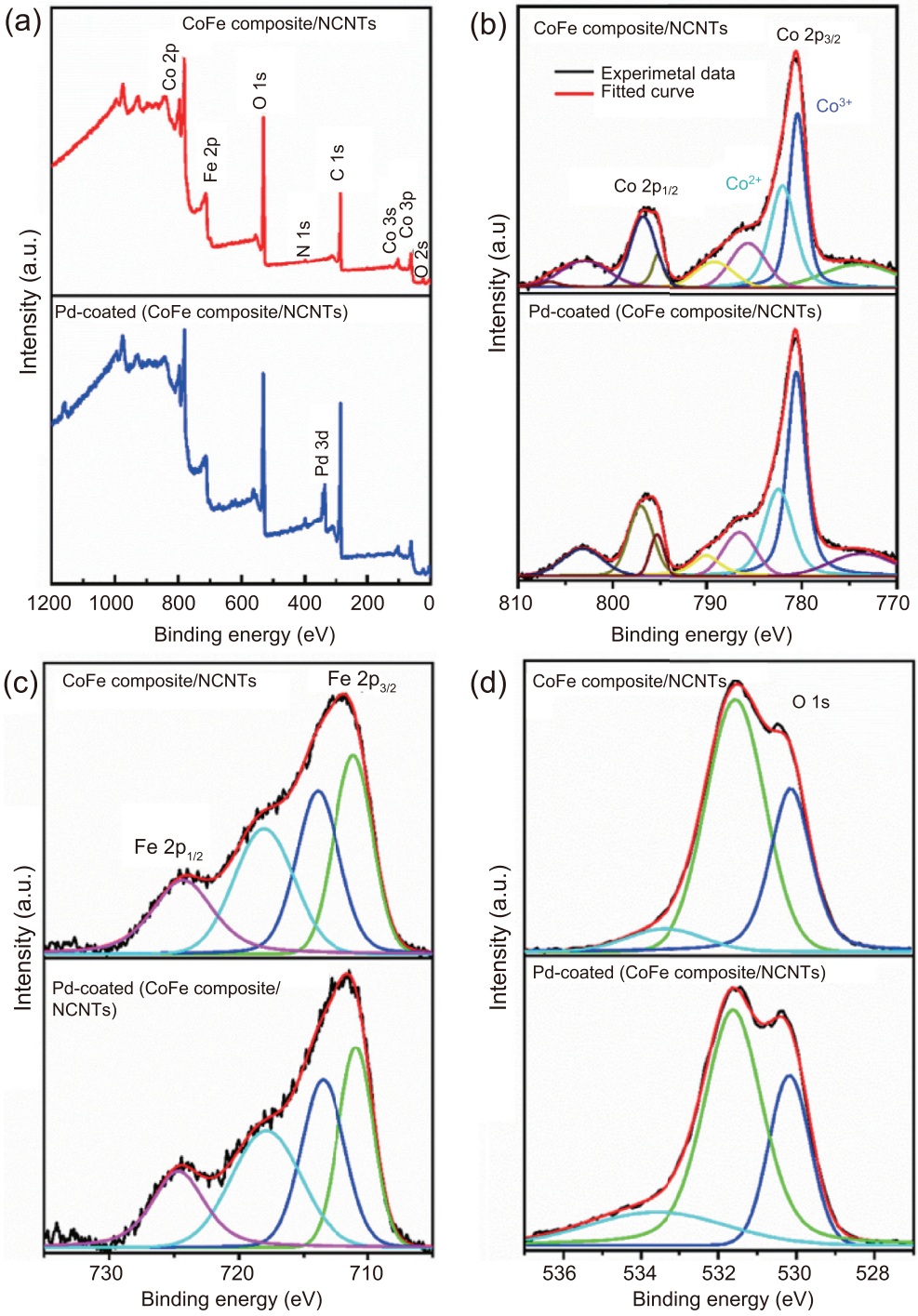

Fig. 2. XPS spectra of CoFe composite/NCNTs and Pd-coated (CoFe composite/NCNTs) (a). High resolution XPS for Co 2p (b), Fe 2p (c), and O 1s of CoFe composite/NCNTs and Pd-coated (CoFe composite/NCNTs) (d), respectively.

was tested. Figs. S3A, B, and C show the LSVs of ORR, OER, and HER activities of $CoFe_2O_4$/NCNTs and CoFe composite/NCNTs catalysts, respectively. Interestingly, the onset potential of CoFe composite/NCNTs is 32 mV lower than that of $CoFe_2O_4$/NCNTs. Similarly, there is a significant reduction in onset potentials for OER (109 mV) and HER (98 mV) for the former catalyst than that of the latter one. The enhanced performance could be ascribed to the synergistic effect of CoFe composite/NCNTs. This can be attributed to the unique CoFe composite structure and its strong interaction with NCNTs to boost electrical conductivity [52]. Besides, both cathodic peak current and onset potentials are further augmented after Pd nanocluster decoration on CoFe composite/NCNTs. Most importantly, the ORR activity of such a Pd-coated (CoFe composite/NCNTs) catalyst is quite comparable with the state-of-the-art Pt/C catalyst. In addition to CV

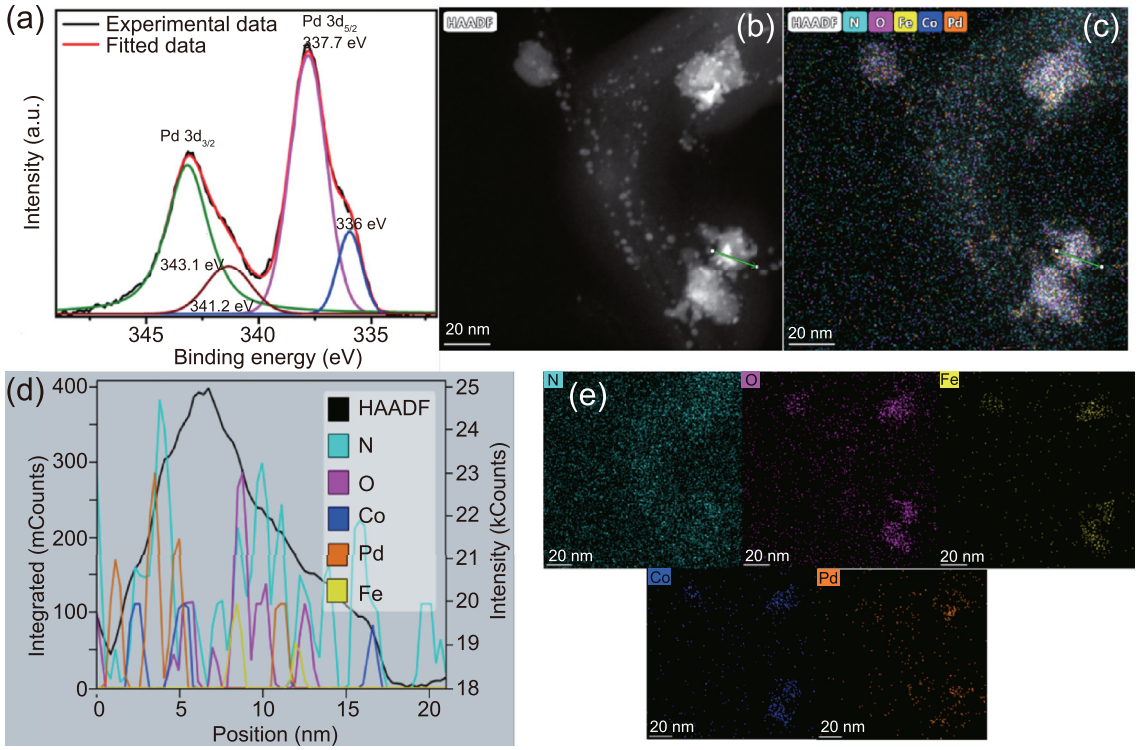

Fig. 3. High resolution XPS for Pd 3d of Pd-coated (CoFe composite/NCNTs) (a). HAADF-STEM images (b and c). Line-scanning profile and EDX elemental mapping of Pd-coated (CoFe composite/NCNTs) (d and e).

analysis, linear sweep voltammetry (LSV) measurements were also carried out, and the obtained results are shown in Fig. 4b. The typical LSV curve of Pd-coated (CoFe composite/NCNTs) catalyst demonstrates a more positive onset potential (E_{onset}) of 897 mV vs. RHE and half-wave potential ($E_{1/2}$) of 828 mV vs. RHE than those of NCNTs, CoFe composite, and CoFe composite/NCNTs samples, which are also comparable to those of commercial Pt/C (E_{onset} = 910 mV and $E_{1/2}$ = 835 mV vs. RHE, respectively). To explore the mechanism of ORR catalyzed by Pd-coated (CoFe composite/NCNTs), the rotating disc electrode (RDE) measurements were also carried out in O_2-saturated 0.1 mol L^{-1} KOH solution at different rotations. The increase in limiting current can be observed with increasing rotation (Fig. 4b), which suggests that the diffusion-limited ORR takes place at Pd-coated (CoFe composite/NCNTs) electrode. The linearity of K-L plots with parallel characteristics of the fitting lines at different potentials (Fig. 4c inset) suggests the first-order reaction kinetics toward the concentration of dissolved O_2. The number of electron transfer involved in the ORR is found to be 3.95 in the potential range of 0.6–0.7 V vs. RHE, calculated from K-L plots, demonstrating that this catalyst can catalyze O_2 reduction through a 4-electron transfer pathway to produce H_2O. The mass transported corrected Tafel slope of Pd-coated (CoFe composite/NCNTs) electrode can be determined to be 90 mV dec^{-1} at 1600 r min^{-1} (Fig. 4d) at low current density (Temkin adsorption) region. This slope is very close and comparable to that of Pt/C catalyst (85 mV dec^{-1}) in similar conditions, demonstrating that the ORR kinetics catalyzed by this catalyst has probably the same one as that catalyzed by Pt/C catalyst.

To further assess the ORR catalytic pathway of the as-prepared catalyst, RRDE measurements were carried out to measure peroxide species (HO_2^-) formed (Fig. 5a) during the ORR process. Fig. 5b depicts the quantity of hydrogen peroxide produced (below 4%) at Pd-coated (CoFe composite/NCNTs) catalyst in the potential range of 0.3–0.8 V, and the number of electrons involved in oxygen reduction was found to be 3.92. Similarly. The RRDE results are in good agreement with RDE measurements, confirming that this Pd-coated (CoFe composite/NCNTs) catalyst can catalyze ORR via a 4-electron route. ORR catalytic pathway of the CoFe composite/NCNTs catalyst was also studied and presented in Fig. S4A. The number of electrons involved in ORR catalyzed by this catalyst was calculated to be 3.66 and ca. 16% hydrogen peroxide produced in the potential range of 0.3–0.7 V (Fig. S4B).

In addition to ORR activity, The OER performance of the prepared catalysts is also examined in the N_2-saturated 1.0 mol L^{-1} KOH electrolyte. Pt/C, Ir/C, CoFe composite/NCNTs, and Pd-coated (CoFe composite/NCNTs) were used as the OER catalysts for comparison. The overpotentials at a current density of 10 mA cm^{-2} and Tafel slope are two key parameters to ascertain the OER activity of catalysts. From Fig. 6a it can be observed that the Pd-coated (CoFe composite/NCNTs) catalyst exhibits a remarkable OER catalytic activity with a lower overpotential (η) of 285 mV at 10 mA cm^{-2} than Pt/C (η = 445 mV), Ir/C (η = 287 mV) and CoFe composite/

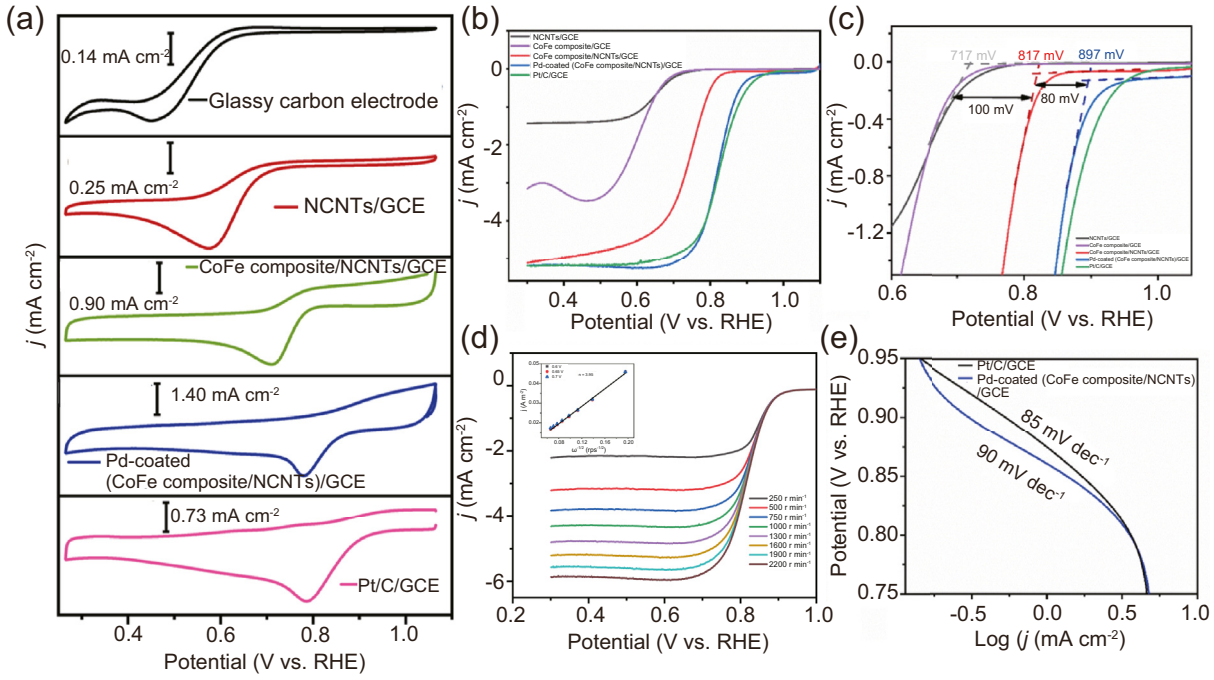

Fig. 4. Cyclic voltammograms (CVs) (a) and linear sweep voltammetry (LSV) polarization curves (1600 r min^{-1}) (b) of different electrodes in O_2-saturated 0.1 mol L^{-1} KOH solution. Onset potentials determination in expanded LSVs (c). LSV curves of Pd-coated (CoFe composite/NCNTs) catalyst at different rotations in O_2-saturated 0.1 mol L^{-1} KOH (d). Tafel slope plots of Pd-coated (CoFe composite/NCNTs) and Pt/C (e).

NCNTs (η = 297 mV). These results suggest that the OER activity of the as-prepared catalyst is even slightly better than that of benchmark Ir/C. Besides, Tafel slopes of Pt/C, Ir/C, CoFe composite/NCNTs, and Pd-coated (CoFe composite/NCNTs) were found to be 158, 91, 48, and 45 mV per decade, respectively (Fig. 6b). Generally, OER can undergo the

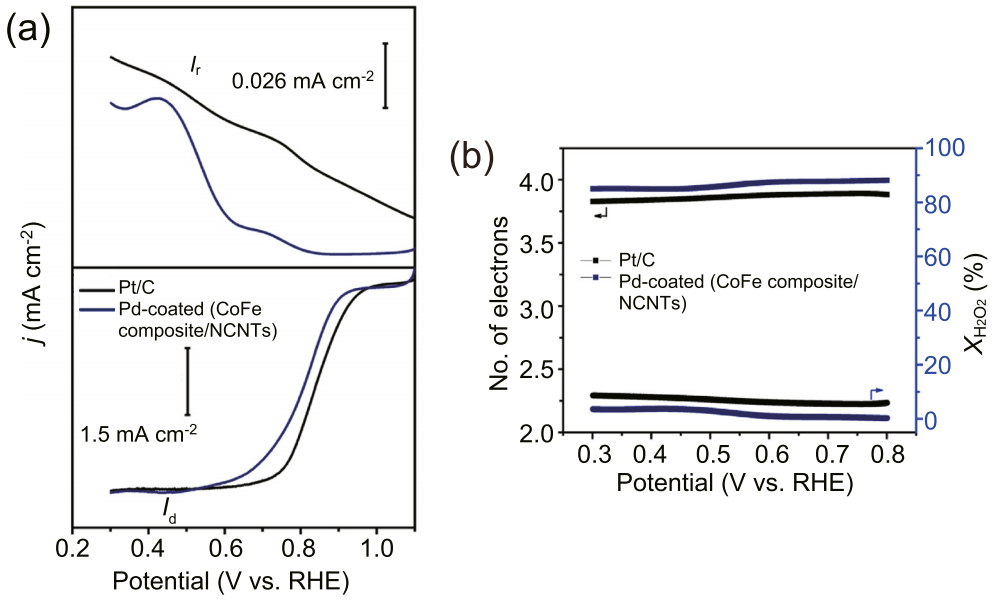

Fig. 5. RRDE polarization curves of Pd-coated (CoFe composite/NCNTs) and Pt/C for ORR at a scan rate of 10 mV s^{-1} at 1600 r min^{-1}. The top part represents H_2O_2 oxidation current at the ring and the oxygen reduction current on the disc illustrated in bottom part (a). Number of electrons transferred and percentage of H_2O_2 produced at Pd-coated (CoFe composite/NCNTs) and Pt/C during ORR (b).

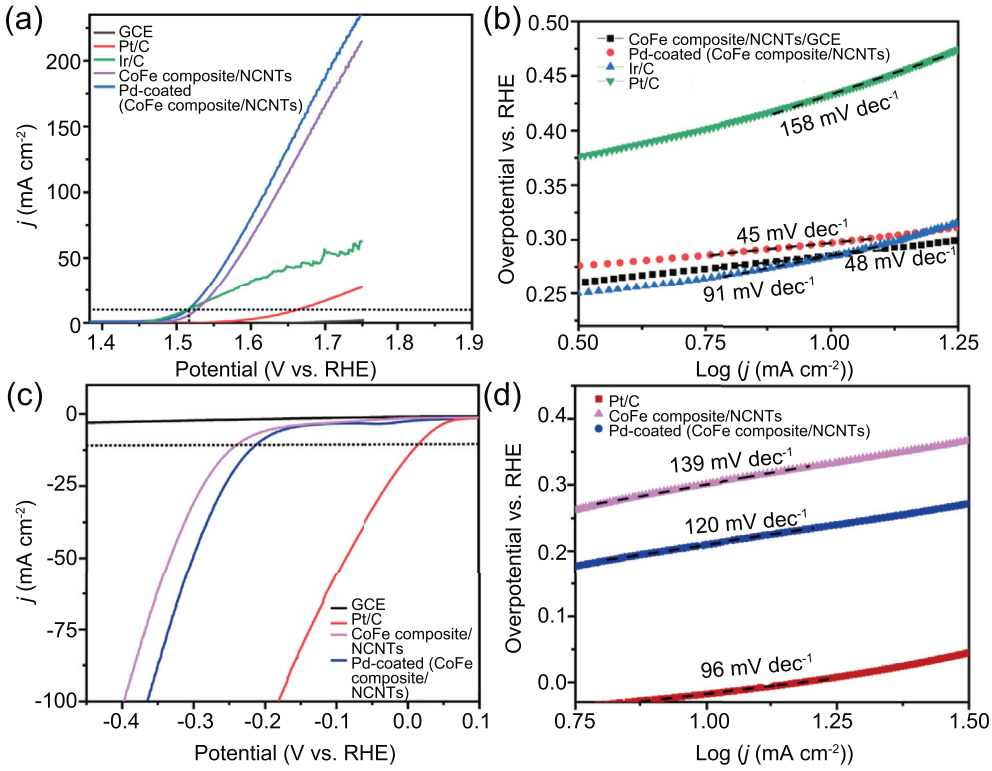

Fig. 6. LSV polarization curves of GCE, Pt/C, Ir/C, CoFe composite/NCNTs, and Pd-coated (CoFe composite/NCNTs) catalysts coated glassy carbon electrodes (GCEs) in N_2-saturated 1.0 mol L^{-1} KOH solution at scan rate of 10 mV s^{-1} (a). The Tafel slopes of Pt/C, Ir/C, CoFe composite/NCNTs, and Pd-coated (CoFe composite/NCNTs) catalysts (b). The Corresponding Tafel slopes of aforementioned catalysts (c). HER performances of GCE, Pt/C, CoFe composite/NCNTs, and Pd-coated (CoFe composite/NCNTs) catalysts in 1.0 mol L^{-1} KOH solution at scan rate of 10 mV s^{-1} (d).

following multiple steps at the active sites of the catalyst in alkaline media [16]:

$$S + OH^- \rightarrow S\text{–}OH_{ads} + e^- \quad (5)$$

$$S\text{–}OH_{ads} + OH^- \rightarrow S\text{–}O_{ads} + H_2O + e^- \quad (6)$$

$$S\text{–}O_{ads} + OH^- \rightarrow S\text{–}OOH + e^- \quad (7)$$

$$S\text{–}OOH + OH^- \rightarrow S + O_2 + H_2O + e^- \quad (8)$$

Where S is a surface-active site of the catalyst.

Among all the catalysts, Pd-coated (CoFe composite/NCNTs) catalyst shows the lowest Tafel slope (45 mV dec^{-1}). Thus, the small Tafel slope of this catalyst reflects fast reaction kinetics, resulting in enhanced catalytic activity. Both experimental and theoretical studies of previous reports [53,54] have confirmed that the decoration of a minimal quantity of precious metals on any material can be conducive to electrocatalysis. For instance, Han et al. [53] reported a high electrocatalytic activity of Pt/CoS_2 supported carbon cloth for OER, which was due to an interfacial coupling between Pt and CoS_2. Consequently, an electron-rich Pt structure with a decrease in its d-band center, resulting in electron-deficient and partially oxidized cobalt species. The higher oxidation state of the Co^{n+} sites is not only beneficial to the electrostatic adsorption of hydroxyl ions but also decreases the energy barrier of S–OOH intermediate formation (Eq. (7)), in turn, conducive OER kinetics. Besides, Zhang et al. [54] explained the high OER activity of an Au/NiFe LDH catalyst based on their previous research facts. Keeping all these points in mind, we believe that the superior ORR, OER activities of the Pd-coated (CoFe composite/NCNTs) catalyst should be due to the interfacial coupling between the components. This hypothesis is confirmed further by XPS analysis. Fig. S5 shows the accelerated degradation study of the catalyst, measured by performing LSV before and after CV cycling tests. Even after 1000 CV cycles, there is no appreciable change in onset potentials as well as the current densities in ORR, OER, and HER LSVs, inferring the catalyst's stable nature.

The prepared catalysts were also subjected to HER tests to assess their activity. Fig. 6c shows the LSV curves of glassy carbon substrate (GCE) electrode, CoFe composite/NCNTs-, Pd-coated (CoFe composite/NCNTs)-, and Pt/C-modified GCE electrodes in 1.0 mol L^{-1} KOH at a scan rate of 10 mV s^{-1}. From the figure it is evident that the bare GCE does not show any electrocatalytic activity for HER, but the CoFe composite/NCNTs- and Pd-coated (CoFe composite/NCNTs)-modified GCEs exhibit low overpotentials of 240 and 214 mV, respectively, to achieve 10 mA cm^{-2} current density. The onset potential is reduced to 145 mV from 178 mV after loading of Pd onto the CoFe composite/NCNTs catalyst. To

compare HER kinetics of the as-prepared catalysts with Pt/C, Tafel slopes were measured as shown in Fig. 6d. In the alkaline environment, typical HER proceeds via three main steps were shown below [53]:

$$S + H_2O + e^- \rightarrow S\text{–}H_{ads} + OH^- \text{ (Volmer adsorption step)} \quad (9)$$

$$S\text{–}H_{ads} + H_2O + e^- \rightarrow S + H_2 + OH^- \text{ (Heyrovsky desorption step)} \quad (10)$$

$$2S\text{–}H_{ads} \rightarrow 2S + H_2 \text{ (Tafel recombination step)} \quad (11)$$

Tafel slopes of CoFe composite/NCNTs, Pd-coated (CoFe composite/NCNTs), and Pt/C catalysts were corresponding to 139, 120, and 96 mV dec^{-1}. It was confirmed in literature [9] that in an alkaline condition, the benchmark Pt/C showed a Tafel slope of 120 mV dec^{-1}. Besides, it followed the Volmer-Heyrovsky route with the Volmer adsorption phase (Eq. (9)) being the rate-determining step. However, in the present work, Pt/C shows a Tafel slope of 96 mV dec^{-1}. Besides, Pd-coated (CoFe composite/NCNTs) catalyst shows a Tafel slope of 120 mV dec^{-1}. Therefore, HER on this catalyst proceeds through the Volmer-Heyrovsky pathway along with Volmer being the rate-determining step [16,53]. Again, appreciable HER activity of Pd-coated (CoFe composite/NCNTs) catalyst could be due to the same reasons which already explained in the OER section. The ORR, OER, and HER results of Pd-coated (CoFe composite/NCNTs) are better/much comparable with previous reports, as tabulated in Table S1.

3.3. The role of catalyst in water electrolysis

Pd-coated (CoFe composite/NCNTs) catalyst was used in electrochemical water splitting experiments in an alkaline medium due to its superior electrocatalytic activity toward OER and HER demonstrated above. The catalyst coated carbon papers (1 cm^2) used as both anode and cathode in a bi-electrode configuration. As shown in Fig. 7a, when cell voltage between anode and cathode reaches above 1.36 V, the current starts to surge spontaneously. The cell voltage reaches to just 1.60 V to achieve 10 mA cm^{-2} current density, which is lower than those reported CoFe LDH-F (1.63 V) [13], NS/rGO-Co4 (1.72 V) [55], $Co_{0.4}Fe_{0.6}$ LDH/g-CN_x (1.61 V) [9], Cu@CoFe LDH (1.68 V) [56] and EG/$Co_{0.85}$Se/NiFe-LDH (1.67 V) [57] catalysts. Fig. 7b shows the chromomeric curve of water electrolyzer catalyzed by Pd-coated (CoFe composite/NCNTs) catalyst at an applied potential of 1.68 V. As shown in the inset of Fig. 7b, both hydrogen and oxygen gases are evolved profusely on catalyst coated cathode and anode electrodes, respectively. Besides, in that applied potential, chronoamperogram is quite stable for more than 20 h. These findings suggest that Pd-coated (CoFe composite/NCNTs) is a promising efficient catalyst for the overall water electrolyzer in alkaline conditions.

3.4. Zn-air battery application

The excellent ORR and OER bifunctional catalytic activity of Pd-coated (CoFe composite/NCNTs) were validated in the Zn-air battery as well. In the present work, the same catalyst was used as a primary, secondary (rechargeable) aqueous Zn-air battery in a flooded mode configuration as well as an all-solid-state flexible air-breathing mode.

3.4.1. Primary aqueous Zn-air battery

A primary Zn-air cell was constructed using a home-made setup which was consisted of a parallel electrode assembly with Pd-coated (CoFe composite/NCNTs) loaded on carbon paper as the cathode, the surface cleansed Zn plate as the anode, and 6.0 mol L^{-1} KOH solution as the electrolyte. As can be seen from the digital photograph (Fig. 8a), the OCV of such a Zn-air battery is 1.47 V, which is very close to commercial Pt/C (1.49 V), very stable up to 12 h (Fig. 8b), and also higher than some previous reports as listed in Table S2. Besides. The obtained OCV is closer to the theoretical one (1.65 V) of the Zn-air battery. Fig. 8c shows the galvanostatic discharge curves of Pd-coated (CoFe composite/NCNTs) air cathode at current densities of 5, 10, 25 and 50 mA cm^{-2}, at which the cell can attain the corresponding cell voltages of 1.35, 1.32, 1.27, and 0.98 V, respectively. Here, two important observations should be described: first, when current density steps down from 50 to 5 mA cm^{-2}, the voltage can revive to 1.33 V, and second, the galvanostatic discharge curve of air cathode at various current densities are superior to that of commercial Pt/C catalyst. At a constant discharge current density of 5 mA cm^{-2}, the cell can be not only stable for a short discharge period but also shows a steady voltage plateau of 1.31 V for more than 55 h (Fig. S6), suggesting stability of the catalyst for ORR. Fig. 8d shows the discharge polarization and the corresponding power density curves. Due to the activation loss, an initial voltage drop could be observed, followed by a subsequent pseudo-linear voltage fall, which is due to the ohmic polarization [44]. The catalyst-based Zn-air battery delivers a peak power density of 261 mW cm^{-2} at a current density of 340 mA cm^{-2}. These results are quite comparable with Pt/C (the maximum power density of 267 mW cm^{-2} @ 310 mA cm^{-2}) as well as previous reports (Table S2). High OCV and the enhanced discharge performance make this catalyst a suitable candidate for primary Zn-air battery application.

3.4.2. Secondary aqueous Zn-air battery

For validating the catalyst developed in this work, a rechargeable Zn-air battery was employed with three-electrode configuration as described elsewhere [58]. In this arrangement, on either side of the Zn plate two separate identical electrodes are placed, one used for charge and the other for discharge. The additional 0.2 mol L^{-1} zinc acetate was added to the conventional 6.0 mol L^{-1} KOH electrolyte in order to facilitate the

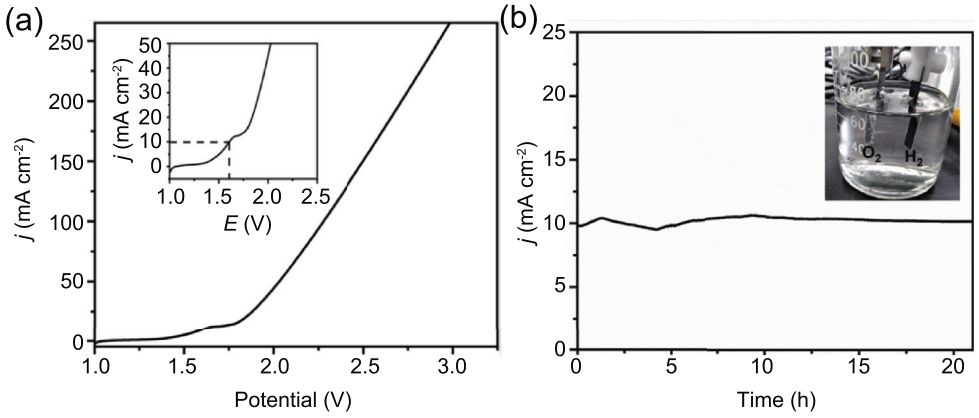

Fig. 7. LSV polarization curve of Pd-coated (CoFe composite/NCNTs) catalyst for both cathode and anode for water electrolysis in 1.0 mol L^{-1} KOH (a). Chronoamperometric measurement of the water electrolysis at the applied potential of 1.68 V, inset shows photograph of the system illustrating the H_2 (right) and O_2 (left) generation due to water electrolysis (b).

reversible deposition of zinc. For comparison studies, a constructed battery consisting of state-of-the-art Pt/C-based electrode for discharge (ORR) and an Ir/C-based electrode for the charge (OER) was used. Fig. 9a shows the charge–discharge profiles of Zn-air batteries consisting of bifunctional Pd-coated (CoFe composite/NCNTs) electrodes (blue curves) and Pt/C + Ir/C electrodes (red curves) in three-electrode setups. The bifunctional catalyst-based battery exhibits the charge–discharge voltage differences of 0.65, 1.03, and 1.44 V at 10, 100, and 200 mA cm^{-2} current densities. Whereas, Pt/C (ORR) and Ir/C (OER) electrodes displayed voltage differences of 0.71, 1.24, and 1.81 V at the corresponding current densities. These results demonstrate that at all three current densities, the as-prepared catalyst outperforms Pt/C and Ir/C by exhibiting lower voltage gaps. Fig. 9b shows the galvanostatic charge–discharge cycles (1 h per cycle) at 10 mA cm^{-2} current density. In the first cycle, the voltage gap of Pd-coated (CoFe composite/NCNTs)-based battery is 690 mV, which is lower

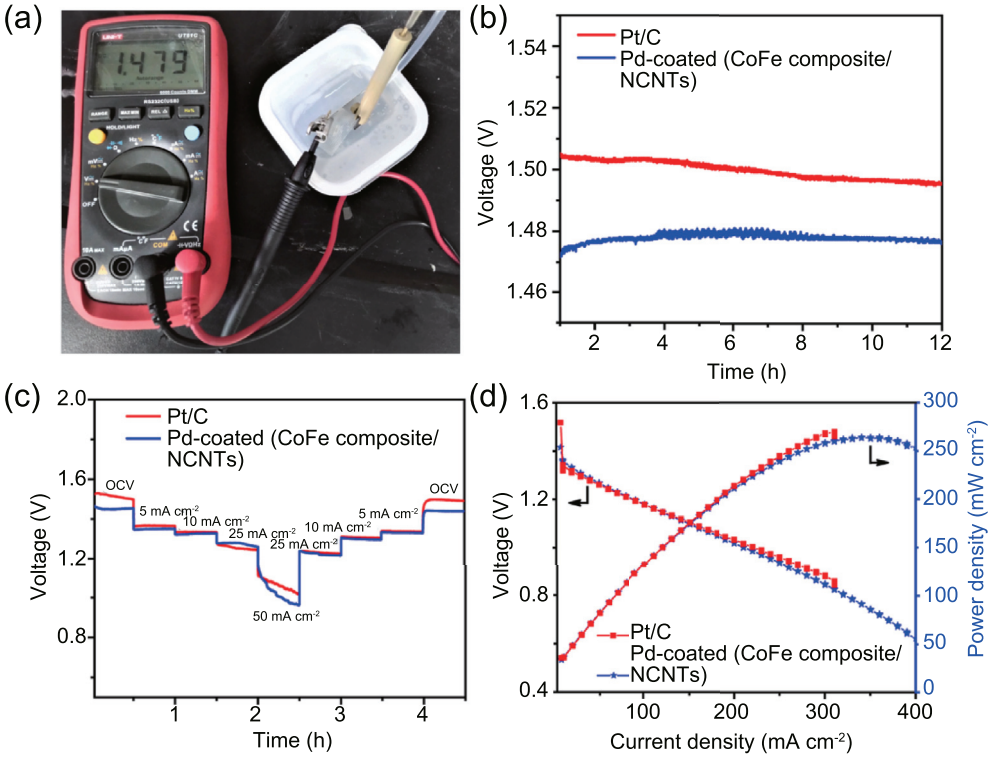

Fig. 8. Photograph of the homemade Pd-coated (CoFe composite/NCNTs) based Zn-air battery showing OCV after assembly at ambient conditions. OCVs of Pd-coated (CoFe composite/NCNTs) and Pt/C based Zn-air batteries (b). Discharge curves of Pt/C and the as-prepared catalysts at various discharge current densities (c). Discharge and power density curves of Pd-coated (CoFe composite/NCNTs) and Pt/C based Zn-air batteries (d).

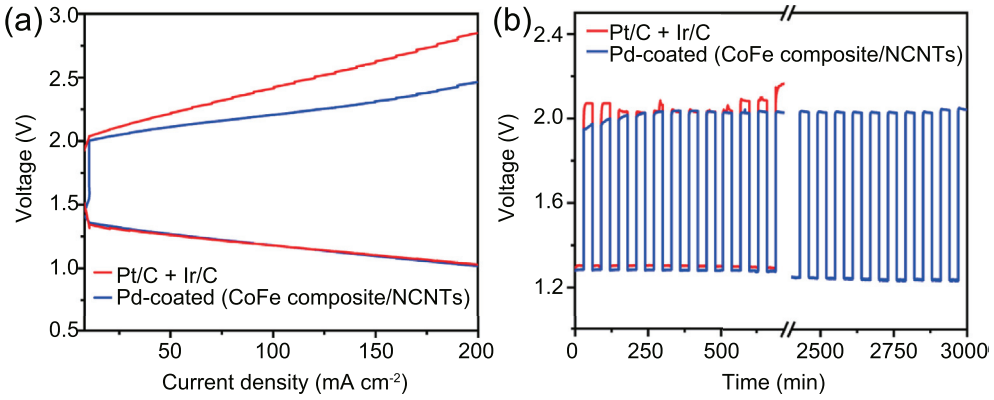

Fig. 9. Charge–discharge polarization curves and galvanostatic charge–discharge profiles of Pd-coated (CoFe composite/NCNTs) and Pt/C + Ir/C electrodes (a). (1 h cycle @10 mA cm^{-2} current density) (b).

than that of Pt/C + Ir/C (760 mV)-based one. Moreover, the latter stops working after 690 min, but the former can run over 3000 min without appreciable change in the voltage gap. Furthermore, Pd-coated (CoFe composite/NCNTs)-based battery displays the roundtrip efficiency of 65% and only 3.5% decrease after 50 cycles (50 h).

3.4.3. All-solid-state flexible Zn-air battery

Based on the validation result that the Pd-coated (CoFe composite/NCNTs)-based Zn-air battery can give outstanding performance in the flooded mode, an all-solid-state flexible Zn-air battery was operated in an air-breathing mode for further validation. As recognized, flexible batteries have

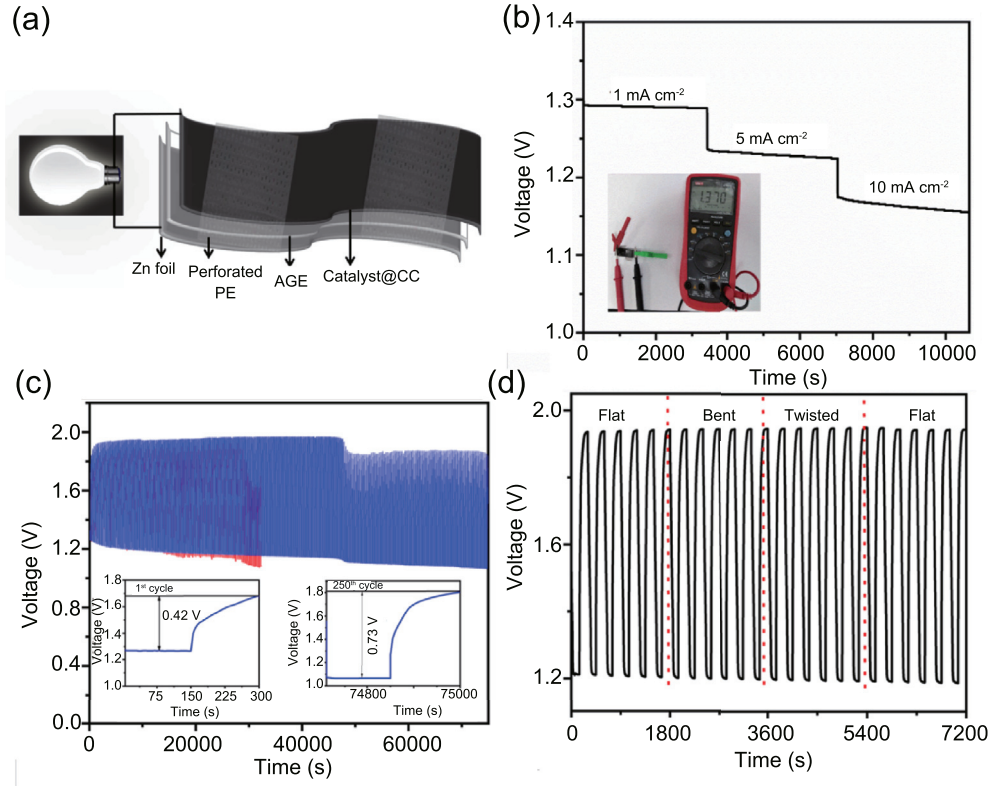

Fig. 10. Schematic representation of fabrication of all-solid-state flexible battery (a). Discharge curves of Pd-coated (CoFe composite/NCNTs) based flexible battery at various discharge current densities (b). Galvanostatic charge–discharge profiles of Pd-coated (CoFe composite/NCNTs) and Pt/C + Ir/C based flexible Zn-air battery systems (5 min cycle@2 mA cm^{-2} current density) (c). Galvanostatic charge–discharge profiles of Pd-coated (CoFe composite/NCNTs) based flexible Zn-air battery at harsh conditions (d).

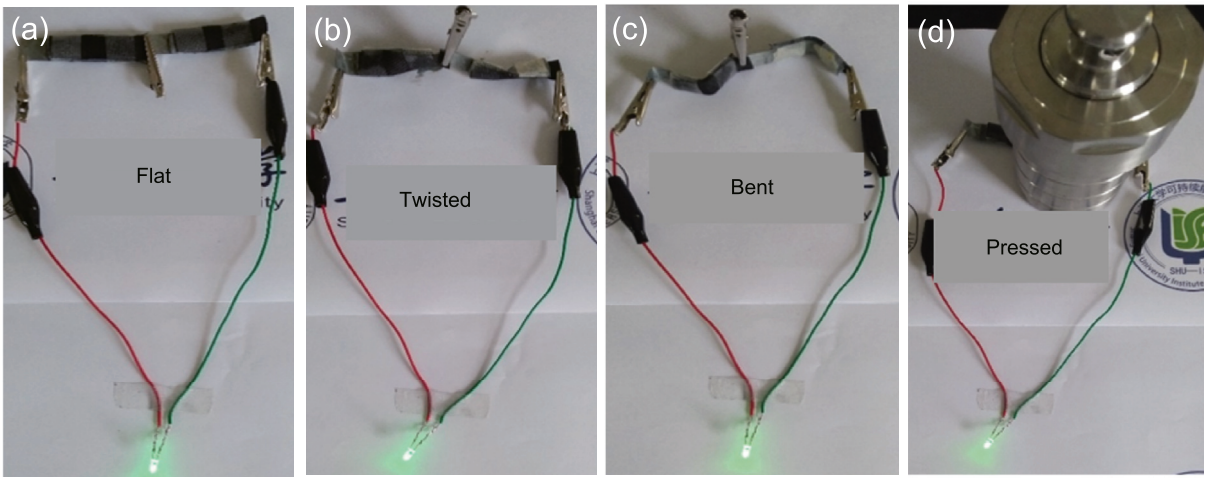

Fig. 11. Photographs of Pd-coated (CoFe composite/NCNTs) based all-solid-state flexible battery working (green LED lighting) at flat, twisting, bending and pressing conditions, respectively (a, b, c, and d).

received tremendous interest because of their increased demand in portable electronic devices. The gel electrolytes used in flexible batteries are comprising the following advantages than flooded mode counterparts [59]: (i) long-life as well as high cycling performance because of low internal resistance and less anodic corrosion, (ii) resistance to anodic dendrite growth, and (iii) no leakage issues, therefore enhanced safety. Fig. 10a shows the schematic of the fabrication process of a flexible Zn-air battery with the as-prepared catalyst and a gel electrolyte. The OCV of such an all-solid-state flexible Zn-air battery comprised of Pd-coated (CoFe composite/NCNTs) air cathode is 1.37 V (Fig. 10b inset), which is higher than SA-PtCoF (1.31 V) [35], MnO_2/$NRGO_{-urea}$ (1.32 V) [19], *h*-FeCo alloy/N-CNFs (1.33 V) [60], and Fe–N-CNTs (1.36 V) [25] based flexible batteries. As can be seen from Fig. 10b, even at air-breathing mode, 1.29, 1.22, and 1.16 V of stable discharge voltage plateaus can be obtained at the applied current densities of 1, 5, and 10 mA cm^{-2}, respectively, suggesting a superior electrocatalytic activity of the catalyst for ORR. The as-prepared catalyst-based solid-state battery delivers a discharge power density of 145 mW cm^{-2} as shown in Fig. S7A, by outperforming some recently published articles [19,25,28,34–36]. In addition, it also delivers a high specific capacity of 587 mAh g^{-1} (Fig. S7B) and energy density of 640 Wh kg^{-1} at 20 mA cm^{-2}, which are normalized to the mass of consumed Zn. Fig. 10c shows the galvanostatic charge–discharge curves of Pt/C + Ir/C and Pd-coated (CoFe composite/NCNTs)-based flexible battery at a current density of 2 mA cm^{-2}. The first charge–discharge voltage plateaus of the batteries are about 1.26 and 1.68 V, respectively, which is corresponding to a voltage gap of 420 mV (Fig. 10c inset) with a round trip efficiency of 75%. After 250 cycles (~21 h), the charge–discharge voltage difference is increased to 730 mV (Fig. 10c inset) with a 59% round trip efficiency retention. However, Pt/C + Ir/C-based flexible battery shows a comparatively good cyclic initially, but it is exhausted completely after 107 cycles. For the flexibility of the battery evaluation, charge–discharge experiments were also carried out in the flat, bending, and twisting positions. As can be seen in Fig. 10d, there is almost no change in voltage profile under these harsh conditions. Furthermore, as a demonstration, LED light is glowed by using Pd-coated (CoFe composite/NCNTs) based flexible batteries in flat, bending, twisting, and pressing conditions, as shown in the digital photographs (Fig. 11), and the corresponding demonstration videos are also given in the supplementary materials. These results confirm that this Pd-coated (CoFe composite/NCNTs) catalyst can be used in flexible batteries with high stability for wearable electronic applications.

4. Conclusions

In summary, Pd-coated (CoFe composite/NCNTs) composite catalyst has been synthesized successfully by a simple coprecipitation and hydrothermal method. NCNTs provide mechanical support to CoFe composite but also are conducive to the latter's electrical conductivity, which in turn improves electrocatalysis performance. Decoration of Pd nanocluster on the composite can not only enhance the utilization of precious metal but also significantly improve ORR, OER, and HER performances. As a result, the as-obtained Pd-coated (CoFe composite/NCNTs) shows superior catalytic ORR ($E_{1/2}$ = 828 mV), OER (η_{j10} = 285 mV), and appreciable HER (η_{j10} = 214 mV) activities in alkaline media, which are comparable to or even better than Pt/C and Pt/C + Ir/C. catalysts. This catalyst-based water electrolysis cell, primary and rechargeable Zn-air battery showed high performance. For instance, in the overall water electrolysis experiment, the cell voltage of such a catalyst coated electrode gives just 1.60 V to achieve 10 mA cm^{-2} current density, which is smaller than previous reports in the literature. Besides, the primary Zn-air battery delivers a constant high OCV of 1.47 V for up to 12 h, and a maximum power density of 261 mW cm^{-2} in the flooded mode configuration. A rechargeable Zn-air battery shows a low charge–discharge voltage gap of 690 mV, which is lower

than that of Pt/C + Ir/C (760 mV)-based counterpart. All-solid-state Zn-air battery constructed by using such a catalyst shows stable 250 charge–discharge cycles without loss of significant round trip efficiency. Most importantly, an all-solid-state Zn-air battery runs very smoothly without a change in voltage gap during flat, bending, and twisting positions. This work not only provides a unique composite as the efficient trifunctional electrocatalyst but also offers its potential applications in overall water electrolyzer and flexible energy devices.

Conflict of interest

The authors declare that they have no known competing financial interests or personal relationships that could have appeared to influence the work reported in this paper.

Acknowledgement

The authors acknowledge the support of the National Nature Science Foundation of China (21908124); Zhaoqing Xijiang Talent Program.

Appendix A. Supplementary data

Supplementary data to this article can be found online at https://doi.org/10.1016/j.gee.2020.12.005.

References

[1] B. Hua, M. Li, Y.F. Sun, Y.Q. Zhang, N. Yan, J. Chen, T. Thundat, J. Li, J.L. Luo, Nanomater. Energy 32 (2017) 247–254.
[2] X. Fan, F. Kong, A. Kong, A. Chen, Z. Zhou, Y. Shan, ACS Appl. Mater. Interfaces 9 (2017) 32840–32850.
[3] Y. Jia, L. Zhang, A. Du, G. Gao, J. Chen, X. Yan, C.L. Brown, X. Yao, Adv. Mater. 28 (2016) 9532–9538.
[4] H. Jiang, J. Gu, X. Zheng, M. Liu, X. Qiu, L. Wang, W. Li, Z. Chen, X. Ji, J. Li, Energy Environ. Sci. 12 (2019) 322–333.
[5] Z. Fu, C. Ling, J. Wang, J. Mater. Chem. A 8 (2020) 7801–7807.
[6] J. Li, Y. Kang, D. Liu, Z. Lei, P. Liu, ACS Appl. Mater. Interfaces 12 (2020) 5717–5729.
[7] X. Long, Z. Wang, S. Xiao, Y. An, S. Yang, Mater. Today 19 (2016) 213–226.
[8] M. Shao, R. Zhang, Z. Li, M. Wei, D.G. Evans, X. Duan, Chem. Commun. 51 (2015) 15880–15893.
[9] T. Bhowmik, M.K. Kundu, S. Barman, ACS Appl. Energy Mater. 1 (2018) 1200–1209.
[10] M. Gong, Y. Li, H. Wang, Y. Liang, J.Z. Wu, J. Zhou, J. Wang, T. Regier, F. Wei, H. Dai, J. Am. Chem. Soc. 135 (2013) 8452–8455.
[11] H. Koshikawa, H. Murase, T. Hayashi, K. Nakajima, H. Mashiko, S. Shiraishi, Y. Tsuji, ACS Catal. 10 (2020) 1886–1893.
[12] F. Song, X. Hu, Nat. Commun. 5 (2014) 4477.
[13] P.F. Liu, S. Yang, B. Zhang, H.G. Yang, ACS Appl. Mater. Interfaces 8 (2016) 34474–34481.
[14] Z. Guo, W. Ye, X. Fang, J. Wan, Y. Ye, Y. Dong, D. Cao, D. Yan, Inorg. Chem. Front. 6 (2019) 687–693.
[15] L. Feng, A. Li, Y. Li, J. Liu, L. Wang, L. Huang, Y. Wang, X. Ge, Chempluschem 82 (2017) 483–488.
[16] J. Guo, J. Sun, Y. Sun, Q. Liu, X. Zhang, Mater. Chem. Front. 3 (2019) 842–850.
[17] F. Song, X. Hu, J. Am. Chem. Soc. 136 (2014) 16481–16484.
[18] D. Lee, H.W. Kim, J.M. Kim, K.H. Kim, S.Y. Lee, ACS Appl. Mater. Interfaces 10 (2018) 22210–22217.
[19] H. Miao, B. Chen, S. Li, X. Wu, Q. Wang, C. Zhang, Z. Sun, H. Li, J. Power Sources 450 (2020) 227653.
[20] Y. Liu, K. Sun, X. Cui, B. Li, J. Jiang, ACS Sustain. Chem. Eng. 8 (2020) 2981–2989.
[21] Y. Xu, P. Deng, G. Chen, J. Chen, Y. Yan, K. Qi, H. Liu, B.Y. Xia, Adv. Funct. Mater. 30 (2020) 1906081.
[22] A. Samanta, C.R. Raj, J. Power Sources 455 (2020) 227975.
[23] K. Kordek, L. Jiang, K. Fan, Z. Zhu, L. Xu, M. Al-Mamun, Y. Dou, S. Chen, P. Liu, H. Yin, P. Rutkowski, H. Zhao, Adv. Energy Mater. 9 (2019) 1802936.
[24] L. Gao, M. Zhang, H. Zhang, Z. Zhang, J. Power Sources 450 (2020) 227577.
[25] Z. Zhang, H. Jin, J. Zhu, W. Li, C. Zhang, J. Zhao, F. Luo, Z. Sun, S. Mu, Carbon N. Y. 161 (2020) 502–509.
[26] M. Wu, G. Zhang, N. Chen, W. Chen, J. Qiao, S. Sun, Energy Storage Mater. 24 (2020) 272–280.
[27] Z. Li, L. Lv, X. Ao, J.G. Li, H. Sun, P. An, X. Xue, Y. Li, M. Liu, C. Wang, M. Liu, Appl. Catal. B Environ. 262 (2020) 118291.
[28] M. Li, F. Luo, Q. Zhang, Z. Yang, Z. Xu, J. Catal. 381 (2020) 395–401.
[29] X. Zhong, W. Yi, Y. Qu, L. Zhang, H. Bai, Y. Zhu, J. Wan, S. Chen, M. Yang, L. Huang, M. Gu, H. Pan, B. Xu, Appl. Catal. B Environ. 260 (2020) 118188.
[30] Q. Feng, Z. Zhao, X.Z. Yuan, H. Li, H. Wang, Appl. Catal. B Environ. 260 (2020) 118176.
[31] C.C. Wang, K.Y. Hung, T.E. Ko, S. Hosseini, Y.Y. Li, J. Power Sources 452 (2020) 227841.
[32] P. Tan, B. Chen, H. Xu, W. Cai, W. He, M. Ni, Appl. Catal. B Environ. 241 (2019) 104–112.
[33] Z. Wang, J. Ang, J. Liu, X.Y.D. Ma, J. Kong, Y. Zhang, T. Yan, X. Lu, Appl. Catal. B Environ. 263 (2020) 118344.
[34] H. Ji, M. Wang, S. Liu, H. Sun, J. Liu, T. Qian, C. Yan, Energy Storage Mater. 27 (2020) 226–231.
[35] Z. Li, W. Niu, Z. Yang, N. Zaman, W. Samarakoon, M. Wang, A. Kara, M. Lucero, M.V. Vyas, H. Cao, H. Zhou, G.E. Sterbinsky, Z. Feng, Y. Du, Y. Yang, Energy Environ. Sci. 13 (2020) 884–895.
[36] X. Shu, S. Chen, S. Chen, W. Pan, J. Zhang, Carbon N. Y. 157 (2020) 234–243.
[37] J. Han, X. Meng, L. Lu, Z.L. Wang, C. Sun, Nanomater. Energy 72 (2020) 104669.
[38] M. Schmid, M. Willert-Porada, Electrochim. Acta 260 (2018) 246–253.
[39] Y. Da, F. Zhao, J. Shi, Z. Zhang, J. Electron. Mater. 49 (2020) 2479–2490.
[40] S. Clark, A.R. Mainar, E. Iruin, L.C. Colmenares, J.A. Blázquez, J.R. Tolchard, Z. Jusys, B. Horstmann, Adv. Energy Mater. 10 (2020) 1903470.
[41] T. Li, Y. Lu, S. Zhao, Z. Da Gao, Y.Y. Song, J. Mater. Chem. A 6 (2018) 3730–3737.
[42] L. Liang, M. Xiao, J. Zhu, J. Ge, C. Liu, W. Xing, J. Energy Chem. 28 (2019) 118–122.
[43] M. Xiao, J. Zhu, J. Ge, C. Liu, W. Xing, J. Power Sources 281 (2015) 34–43.
[44] V.G. Anju, R. Manjunatha, P.M. Austeria, S. Sampath, J. Mater. Chem. A 4 (2016) 5258–5264.
[45] Y. Zhang, Y. Liu, C. Fei, Z. Yang, Z. Lu, R. Xiong, D. Yin, J. Shi, J. Appl. Phys. 108 (2010) 084312.
[46] M. Yeganeh Ghotbi, A. Javanmard, H. Soleimani, Sci. Rep. 8 (2018) 23–25.
[47] Y. Zhao, R. Nakamura, K. Kamiya, S. Nakanishi, K. Hashimoto, Nat. Commun. 4 (2013) 2390.
[48] M. Zhao, Y. Cao, X. Liu, J. Deng, D. Li, H. Gu, Nanoscale Res. Lett. 9 (2014) 142.

[49] X. Wang, J. Chen, J. Zeng, Q. Wang, Z. Li, R. Qin, C. Wu, Z. Xie, L. Zheng, Nanoscale 9 (2017) 6643–6648.
[50] A.I. Boronin, E.M. Slavinskaya, I.G. Danilova, R.V. Gulyaev, Y.I. Amosov, P.A. Kuznetsov, I.A. Polukhina, S.V. Koscheev, V.I. Zaikovskii, A.S. Noskov, Catal. Today 144 (2009) 201–211.
[51] K. Gandha, K. Elkins, N. Poudyal, J. Ping Liu, J. Appl. Phys. 117 (2015) 2–6.
[52] X. Zhang, Y. Wang, S. Dong, M. Li, Electrochim. Acta 170 (2015) 248–255.
[53] X. Han, X. Wu, Y. Deng, J. Liu, J. Lu, C. Zhong, W. Hu, Adv. Energy Mater. 8 (2018) 1870110.
[54] J. Zhang, J. Liu, L. Xi, Y. Yu, N. Chen, S. Sun, W. Wang, K.M. Lange, B. Zhang, J. Am. Chem. Soc. 140 (2018) 3876–3879.
[55] N. Wang, L. Li, D. Zhao, X. Kang, Z. Tang, S. Chen, Small 13 (2017) 1701025.
[56] L. Yu, H. Zhou, J. Sun, F. Qin, D. Luo, L. Xie, F. Yu, J. Bao, Y. Li, Y. Yu, S. Chen, Z. Ren, Nanomater. Energy 41 (2017) 327–336.
[57] Y. Hou, M.R. Lohe, J. Zhang, S. Liu, X. Zhuang, X. Feng, Energy Environ. Sci. 9 (2016) 478–483.
[58] Y. Li, M. Gong, Y. Liang, J. Feng, J.E. Kim, H. Wang, G. Hong, B. Zhang, H. Dai, Nat. Commun. 4 (2013) 1805.
[59] B. Roy, K.J. Shebin, S. Sampath, J. Power Sources 450 (2020) 227661.
[60] Y. Ma, W. Zang, A. Sumboja, L. Mao, X. Liu, M. Tan, S.J. Pennycook, Z. Kou, Z. Liu, X. Li, J. Wang, Sustain. Energy Fuels 4 (2020) 177–1753.